Passive imaging with pulsed ultrasound insonations

Kevin J. Haworth[a)]
Department of Internal Medicine, Division of Cardiovascular Diseases, University of Cincinnati, Cincinnati, Ohio

T. Douglas Mast and Kirthi Radhakrishnan
Biomedical Engineering Program, University of Cincinnati, Cincinnati, Ohio

Mark T. Burgess and Jonathan A. Kopechek
Department of Mechanical Engineering, Boston University, Boston, Massachusetts

Shao-Ling Huang and David D. McPherson
Department of Internal Medicine, University of Texas Health Science Center at Houston, Houston, Texas

Christy K. Holland
Department of Internal Medicine, Division of Cardiovascular Diseases, University of Cincinnati, Cincinnati, Ohio

(Received 9 November 2011; revised 23 May 2012; accepted 25 May 2012)

Previously, passive cavitation imaging has been described in the context of continuous-wave high-intensity focused ultrasound thermal ablation. However, the technique has potential use as a feedback mechanism for pulsed-wave therapies, such as ultrasound-mediated drug delivery. In this paper, results of experiments and simulations are reported to demonstrate the feasibility of passive cavitation imaging using pulsed ultrasound insonations and how the images depend on pulsed ultrasound parameters. The passive cavitation images were formed from channel data that was beamformed in the frequency domain. Experiments were performed in an *in vitro* flow phantom with an experimental echo contrast agent, echogenic liposomes, as cavitation nuclei. It was found that the pulse duration and envelope have minimal impact on the image resolution achieved. The passive cavitation image amplitude scales linearly with the cavitation emission energy. Cavitation images for both stable and inertial cavitation can be obtained from the same received data set.
 [http://dx.doi.org/10.1121/1.4728230]

PACS number(s): 43.80.Vj, 43.60.Fg, 43.35.Ei, 43.60.Jn [ADP] Pages: 544–553

I. INTRODUCTION

Acoustic cavitation has been identified as an important mechanism in many therapeutic ultrasound applications, including drug and gene release and delivery,[1–5] sonothrombolysis,[6–10] sonophoresis,[11–13] hemostasis,[14] and thermal ablation.[15,16] Current research focuses on increasing efficacy and illuminating the specific mechanisms by which acoustic cavitation induces a bioeffect. Many passive and active cavitation detection techniques[17–19] have been developed to monitor acoustic cavitation.

Passive cavitation detection uses a transducer that operates passively (i.e., no transmit) to listen for ultrasound emissions from a cavitation event. Its primary asset is that the measurement technique does not affect the cavitation source. Furthermore, the detected signals can be post-processed to determine frequency components, which are corrected for the frequency response of the detector. The different frequency components have been associated with different types of cavitation activity. Emissions below 50 kHz have been associated with boiling.[20,21] Detection of emissions at the subharmonic (one-half the driving frequency) and ultraharmonic (odd harmonics of the subharmonic) bands at a power level greater than that detected in the inharmonic bands is an indication of stable cavitation within an insonified bubble population.[21–26] Inertial cavitation results in substantial broadband emissions.[21,22] However, some low-level broadband emissions may also result from stable cavitation, due to random bubble motion without inertial collapse, while some subharmonic emissions may result from large-amplitude bubble oscillations preceding inertial collapse.[25]

The study presented here follows recent convention[21,26] by identifying broadband emissions primarily with inertial cavitation and ultraharmonic emissions primarily with stable cavitation. Since inertial cavitation emissions are primarily broadband, while stable cavitation emissions are primarily narrow-band, one can quantify emission energy at inharmonic frequencies to distinguish stable cavitation from inertial cavitation. Inharmonic frequency bands are defined as those bands that do not contain the fundamental, harmonic, subharmonic, or ultraharmonic frequencies. Within an insonified population, some bubbles may cavitate stably while others cavitate inertially.

Until recently, most passive cavitation detectors (PCDs) were either focused or unfocused, single-element transducers.

[a)]Author to whom correspondence should be addressed. Electronic mail: kevin.haworth@uc.edu

 0001-4966/2012/132(1)/544/10/$30.00

Using a single-element transducer requires a trade-off between the spatial specificity and spatial sensitivity of the detection region. Focused PCDs provide high sensitivity and spatial specificity in the focal region but are insensitive outside the focal region.[18,27] Unfocused PCDs can record cavitation emissions over a large area but have decreased sensitivity and spatial specificity.[28,29]

More recently, PCDs using multiple-element arrays have been shown to reduce the limitations of focused and unfocused PCDs by allowing for spatial resolution over a large area. Farny *et al.*[23] and Salgaonkar *et al.*[30] used modified diagnostic scanners with the ultrasound array transmit turned off and the array in a passive detection state. The cavitation was induced by a separate therapy transducer. The scanner beamformed the "receive-only" radio-frequency (RF) signals. Beamformed RF signals were post-processed offline to estimate frequency components and types of cavitation activity in a spatially resolved manner, creating a passive cavitation image (PCI). Salgaonkar *et al.*[30] referred to these images as passive cavitation maps. In addition to experimental demonstration, Salgaonkar *et al.*[30] provided a model for idealized passive imaging with single-frequency (i.e., continuous-wave) insonations and a model for the spatial sensitivity patterns of the diagnostic scanner used in their experiments. Both the modeling and experimental data showed significantly better azimuthal resolution than range resolution. Farny *et al.*[23] were able to show cavitation activity at the same location as they observed B-mode hyperechoic regions after insonation. Salgaonkar *et al.*[30] showed cavitation activity within the beam profile of the insonation transducer.

Gyöngy *et al.*[31,32] and Jensen *et al.*[33] have taken a very similar approach, but employed non-beamformed data from each element of a diagnostic ultrasound scanner array that was demodulated and basebanded to in-phase and quadrature (I/Q) data. The non-beamformed I/Q data was processed using time exposure acoustics,[34] which is a delay, sum, and integrate algorithm. This technique is very similar to the algorithm employed by the scanner with subsequent offline processing used by Salgaonkar *et al.*[30] Gyöngy *et al.* perform a digital delay and sum, while Salgaonkar *et al.* perform an analog delay and sum. Also, the time exposure acoustics algorithm used by Gyöngy *et al.*[31,32] worked with time-domain data, whereas Salgaonkar *et al.*[30] worked with frequency-domain data offline. Time-domain processing has the advantage of reduced computational load and could be easier to implement on current clinical scanners, which use similar processes (delay and sum). However, frequency-domain processing allows one to differentiate between different classes of cavitation conveniently. One can select the approach based on the specific requirements of the experiment.

The experimental work of Gyöngy *et al.*[32,35] showed transient but periodic cavitation events during continuous-wave insonation. Therefore published results have indicated that passive cavitation imaging of pulsed and continuous sources is possible. However, the dependence of the PCI point spread function on the cavitation emission duration and envelope is unknown. Delay and sum B-mode imaging has a strong dependence of image quality on pulse duration, indicating that a delay, sum, and integrate imaging algorithm may also depend on pulse duration and bandwidth. Through experiment and simulation, the work reported within this manuscript explores the effect of pulse duration and pulse envelope on the resolution of passive cavitation imaging. The role of the frequency bands used to form the cavitation image and array apodization will also be elucidated.

II. METHODS

A. Beamforming algorithm

Cavitation emissions were obtained on multiple passive elements simultaneously. The received emissions were beamformed using a delay, sum, and integrate algorithm similar to Salgaonkar *et al.*[30] and Gyöngy *et al.*[31,32] The algorithm performs delay-and-sum beamforming based on the time of flight from an image location (pixel) to a given element. After summing over the channel number, the frequency-dependent energy in the summed waveform was computed and used to assign a pixel value at that location. The frequency dependent image, $B(\omega, \vec{x})$, is defined in Eq. (1). Figure 1 shows the relationship between an image location $\vec{x}$ and the array.

$$B(\omega,\vec{x}) = \left| \sum_{n=1}^{N} S_n(\omega) A(\vec{x}_n,\vec{x},S_n) \exp\left(i\omega \frac{|\vec{x}_n - \vec{x}|}{c} \right) \right|^2, \tag{1}$$

where $S_n(\omega)$ is the frequency domain representation of the signal received on the nth element of the passive array located at $\vec{x}_n$ and $A(\vec{x}_n, \vec{x}, S_n)$ is an optional apodization that can be applied. As noted by Norton and Won,[34] this algorithm results in a bias that can be removed by subtracting the total energy of the individual channels. A passive cavitation image for each frequency, $I(\omega,\vec{x})$, was formed as

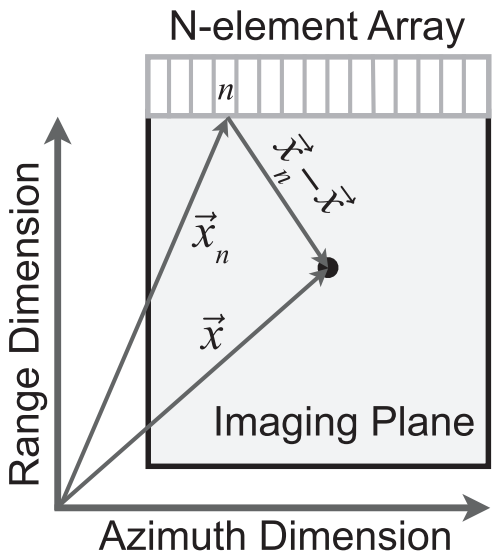

FIG. 1. Schematic of passive imaging array and corresponding imaging plane. The nth element of the array is labeled and the black dot indicates image location $\vec{x}$. The elevational direction is out of the plane of the page.

$$I(\omega, \vec{x}) = B(\omega, \vec{x}) - \sum_{n=1}^{N} |S_n(\omega)\, A(\vec{x}_n, \vec{x}, S_n)|^2. \quad (2)$$

The final PCI, $I(\vec{x})$, was formed by summing over the frequency bands corresponding to the cavitation mode of interest (e.g., subharmonic and ultraharmonic bands for stable cavitation or the inharmonic portion of the broadband band for inertial cavitation). Unlike traditional delay-and-sum algorithms, absolute time-of-flight information for the summed waveform was not used to determine image depth. This strategy avoids making an assumption about what temporal portion of a pulse induced a cavitation event or if the cavitation event occurred post-insonation.[28,36] McLaughlan *et al.* investigated using B-mode imaging, which incorporates absolute time-of-flight information.[21] The resulting images showed interference patterns with little or no spatial correspondence to the location of cavitation, though B-mode images were a useful metric for determining when cavitation occurred.

It should be noted that images formed from Eq. (2) are based on the signal received by each element. In general, this algorithm can be used to beamform passively any scattered signals, not just cavitation emissions. When beamforming frequency bands that are only produced via cavitation emissions, such as subharmonics, ultraharmonics, and inharmonics, the resulting image would be a passive cavitation image. However when beamforming other frequency bands, such as harmonics that can be produced via nonlinear propagation, non-linear tissue scattering, or cavitation emissions, one can no longer *a priori* state the exact type of passive image produced (e.g., passive field-map image, passive scattering image, or passive cavitation image). For the remainder of this paper we will refer to all passive images as passive cavitation images, even though in some cases the signal may not be from a cavitation event.

Four different apodization functions were investigated:

$$A_{\text{Unity}}(\vec{x}_n, \vec{x}, S_n) = 1, \quad (3a)$$

$$A_{\text{Cos}}(\vec{x}_n, \vec{x}, S_n) = \frac{\vec{x} \cdot \vec{x}_n}{|\vec{x}||\vec{x}_n|}, \quad (3b)$$

$$A_{\text{Norm}}(\vec{x}_n, \vec{x}, S_n) = \frac{1}{\sqrt{|\sum_{\omega'} S_n(\omega')|^2}}, \quad (3c)$$

$$A_{\text{Norm Cos}}(\vec{x}_n, \vec{x}, S_n) = \frac{A_{\text{Cos}}(\vec{x}_n, \vec{x}, S_n)}{\sqrt{|\sum_{\omega'} S_n(\omega')|^2}}. \quad (3d)$$

A_{Unity} represents no modification to the received signals. A_{Cos} is a cosine apodization to reduce grating lobes (obtained from the dot product of $\vec{x}$ and $\vec{x}_n$ and normalizing by their magnitudes). A_{Norm} scales the amplitude of each channel so that all channels have equal root-mean-square values. For arrays where the element sensitivity falls off with increasing angle, the array f-number is effectively increased. Using A_{Norm} decreases the f-number, which typically improves resolution. This may also more accurately represent the signal from omnidirectional scatterers. A_{NormCos} applies both the root-mean-square normalization and cosine apodization.

To compare the passive images for the different pulse durations, pulse envelopes, and apodizations, all PCIs, except where noted, were normalized using the following equation:

$$I_{\text{norm}}(\vec{x}) = \frac{I(\vec{x})}{\max[I(\vec{x})]}. \quad (4)$$

B. Experiment

Passive cavitation images from experimentally obtained data were formed using Eq. (2). A schematic of the experimental setup is seen in Fig. 2. Signals in the frequency domain, $S_n(\omega)$, were obtained by insonifying an experimental ultrasound contrast agent, echogenic liposomes (ELIP),[37,38] in a flow phantom with spectral Doppler pulses (center frequency of 6 MHz) from a CL15-7 transducer driven by an HDI-5000 clinical scanner (Philips Medical Systems, Bothell, WA). The acoustic properties and morphology of ELIP have been recently studied by Kopechek *et al.*[39] and Paul *et al.*[40] ELIP are of interest for both their diagnostic[37,38,41,42] and therapeutic[43–47] capabilities. The flow phantom consisted of a reservoir connected to a peristaltic pump (Rabbit, Rainin, Oakland, CA), which pumped a solution of ELIP (0.1 mg/ml lipid concentration) in 0.5% (wt./vol) bovine serum albumin (Sigma-Aldrich Co., St. Louis, MO) in phosphate buffered saline (Sigma-Aldrich Co.), through a low-density polyethylene tube (2.7 mm inner diameter, 4.0 mm outer diameter, McMaster-Carr, Aurora, OH) at a 2.0 mL/min flow rate. The portion of the tube insonified was submerged in a tank of 22 °C degassed water (dissolved oxygen of <30%) to minimize the occurrence of cavitation outside the tube. After the insonation zone, the ELIP emptied into a waste reservoir. B-mode images were used to align the L8-3 transducer with the polyethylene tube by obtaining a uniform echogenicity from the tube wall along the length of

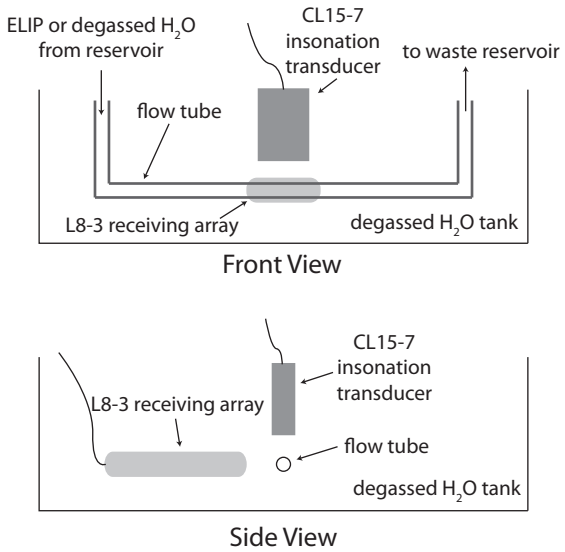

FIG. 2. Schematic of the experimental setup. A single-pass flow phantom with ELIP in a polyethylene tube was used. The ELIP were insonified by the CL15-7 transducer and cavitation emissions were recorded passively with the L8-3 transducer passive array.

the tube and orienting the tube parallel to the face of the transducer, as can be seen in Fig. 3. Subsequently the CL15-7 transmitted Doppler pulses that scattered off the tube at the center of the CL15-7 B-mode image. The L8-3 was shifted azimuthally until the scatter was centered in its B-mode image. The CL15-7 was aligned in the same manner using B-mode images.

ELIP were manufactured at the University of Texas Health Science Center at Houston and shipped as a lyophilized powder to the University of Cincinnati where they were reconstituted and injected into the flow model. Huang *et al*. established the manufacturing protocol for the ELIP.[37] The ratio of lipids used was determined by Buchanan *et al*.[38] and was 42:27:8:8:15 of 1,2-dipalmitoyl-sn-glycero-3-phosphocholine (DPPC) to L-a-phosphatidylcholine (egg-PC) to 1,2-dipalmitoyl-sn-glycero-3-phosphoethanolamine (DPPE) to 1,2-dipalmitoyl-sn-glycero-3-[phosphor-rac-1-gly-cerol] (DPPG) to cholesterol. All lipids were purchased from Avanti Polar Lipids (Alabaster, AL).

The insonation spectral Doppler pulse duration and envelope from the CL15-7 were measured in the free field at the location where the polyethylene tube was placed. The pulses were measured using a 0.2 mm needle hydrophone attached to a 3D-micropositioning system. Both the pulse duration and envelope changed when the on-screen spectral Doppler "sample volume" setting was changed. While called a sample volume on the scanner, it was reported on-screen with units of length. For sample volume values of 5.0 mm (3.33 μs) or less, the pulse envelope, as observed with the hydrophone was similar to a Gaussian. For displayed sample volume values of 7.5 mm (5.0 μs) or larger, the pulse envelope was a rectangular window. It should be noted that while the insonation pulse duration and envelope can be controlled experimentally, the cavitation emission pulse duration and envelope cannot be controlled with the same ease and precision. Furthermore, the spatial distribution of microbubbles continually changes as the ELIP flow through the tube and therefore the spatial distribution of cavitation activity would be expected to change. Therefore to observe the impact of passively imaging different known pulse durations and envelopes, the ELIP solution was replaced with filtered, deionized, and degassed water. Using this water, no energy was observed above the system noise floor in the subharmonic or inharmonic bands. Therefore, in this case, the passive imaging corresponded to scattering from the tube walls, which were stationary in time and space.

Received signals, $S_n(\omega)$, were obtained using the IQscan research package on a z.one ultra scanner with an L8-3 transducer (ZONARE Medical Systems, Inc., Mountain View, CA).[48,49] The array had a 0.3 mm pitch, 6 mm element height, 25 mm elevational focus, 128 elements, and no inter-element apodization. Using the research package, the signals received by the center 64 elements were recorded in parallel for 138 μs. This constituted one frame of RF data. The z.one ultra scanner preprocessed each frame of RF data by preamplifying by 30 dB (flat across frequency and time) and basebanding to I/Q data. To prevent aliasing, a 2–7 MHz bandpass filter was used. The I/Q data was beamformed offline using MATLAB (Mathworks, Natick, MA) to produce the PCI, $I(x)$. It should be noted that there was no temporal synchronization between the CL15-7 pulse Doppler firings and the L8-3 frame recordings. The Doppler pulse repetition frequency was 1250 Hz. The L8-3 frame rate (1124 Hz) was selected so that at least every ninth frame would capture a cavitation event. When forming passive cavitation images, those frames that captured no cavitation or scattering had an order of magnitude or smaller total energy in the frame as compared to frames with cavitation or scattering. Therefore, they could easily be excluded from analysis. Forty-five PCIs were then averaged pixel-by-pixel on a linear scale to form a final PCI that provides a representative image of the average cavitation activity. The final averaged PCI was converted to a dB scale for display.

For each run, before placing the L8-3 transducer into a passive state, the L8-3 was used to capture a B-mode image to record any echo-contrast destruction from the CL15-7 Doppler pulses. The L8-3 was then put into a passive state and recorded cavitation emissions at the Doppler exposure settings used to capture the B-mode images. The PCIs were overlaid on the corresponding B-mode images using the "alpha transparency" figure property in MATLAB. The PCI pixel transparency, $\alpha(\vec{x})$, was set by

$$\alpha(\vec{x}) = \left(\log_{10}\left[\frac{I(\omega,\vec{x})}{\max[I(\omega,\vec{x})]}\right]\right)^{1/3}. \quad (5)$$

C. Simulation

For the experimental setup described above, it was not possible to control pulse duration and pulse envelope independently. Furthermore, the pulse duration was limited to 8.33 μs. Therefore simulations were used to study the effect of pulse duration and pulse envelope independently and to study pulse durations extending from two-cycles to continuous-wave. Simulated passive cavitation images were formed based on Eq. (2). To produce a signal, $S_n(\omega)$, a source waveform was defined and numerically propagated from a preselected source location, $\vec{x}_s$. The source waveforms were created from sinusoids multiplied by a rectangular or modified Gaussian temporal window. The rectangular windows had an amplitude of one. The duration was varied between one-half cycle and 828 cycles. A duration of 828 cycles at 6 MHz corresponds to 138 μs, which is the longest duration the z.one ultra scanner could record RF data for during one frame. Therefore, when compared to the experimental data, 828 cycles effectively approximates a continuous-wave emission. For each rectangular window, a corresponding Gaussian window was defined by setting the Gaussian peak amplitude to one and the width defined such that the total energy in the pulse was the same as in the rectangularly window source. Propagation was performed in the frequency domain by multiplying the emission waveform with a propagation vector for each element. Assuming spatial reciprocity, the propagation vector was computed as the impulse response from an array element to the location of simulated cavitation emission based on the diffracted spherical-wave Fresnel approximation.[50] The simulated array parameters were the same as the L8-3 transducer. An empirically obtained spatial apodization

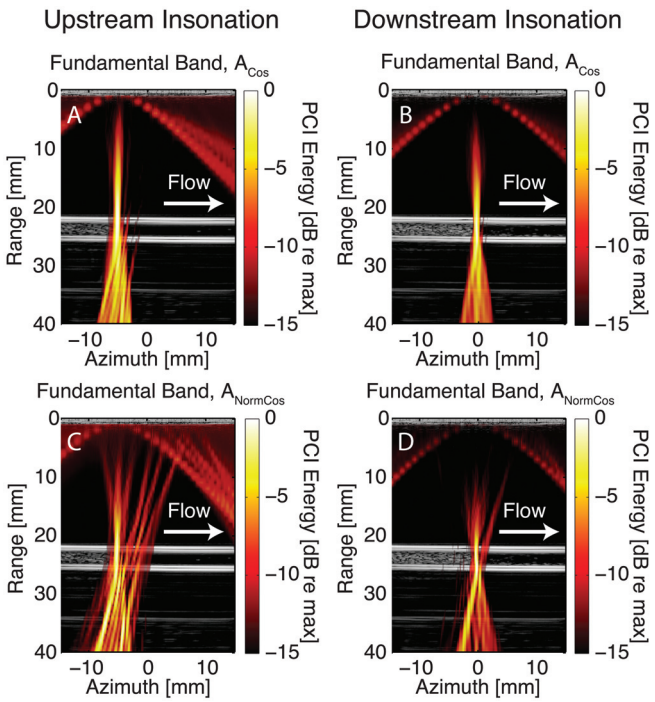

FIG. 3. PCI overlaid (hot colormap) on a B-mode (grayscale) for the spectral Doppler "sample volume" placed at an upstream location [(A) and (C)] and a location 5 mm downstream [(B) and (D)]. The PCI was beamformed over the fundamental frequency band (5.85–6.15 MHz) using A_{Cos} [(A) and (B)] and A_{NormCos} [(C) and (D)]. ELIP were insonified with an MI of 0.8 and pulse duration of 1.33 μs.

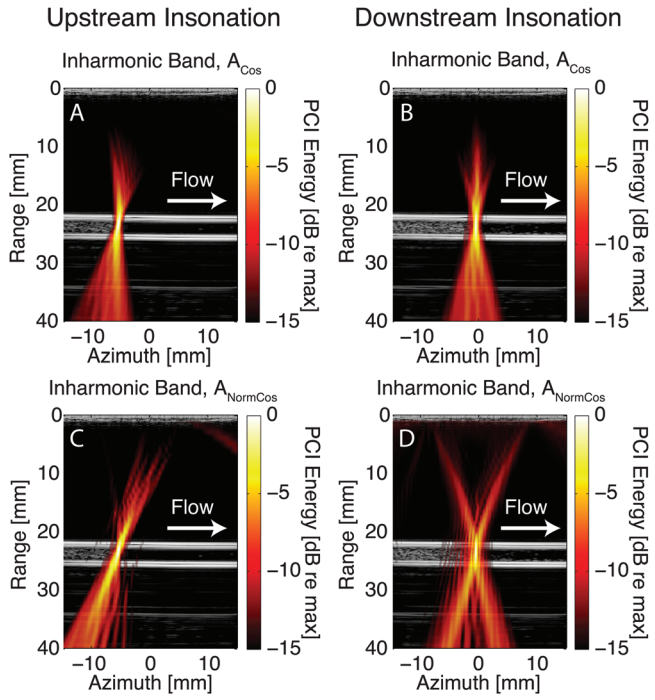

FIG. 4. PCI overlaid (hot colormap) on a B-mode (grayscale) for the spectral Doppler "sample volume" placed at an upstream location [(A) and (C)] and a location 5 mm downstream [(B) and (D)]. The PCI was beamformed over the inharmonic frequency band (2.85–3.15 MHz) using A_{Cos} [(A) and (B)] and A_{NormCos} [(C) and (D)]. ELIP were insonified with an MI of 0.8 and pulse duration of 1.33 μs.

was applied to each channel so that the root-mean-square (RMS) value of the received signal on each element was the same as the average RMS values on experimentally-obtained signals. The data was then apodized according to Eq. (3a). Passive cavitation image beam widths for different pulse duration and envelopes were compared.

III. RESULTS

A. Experiment: Apodization and localization

Figures 3 and 4 show passive cavitation images overlaid on corresponding B-mode images for the pulse Doppler sample volume placed at an upstream or downstream location. The downstream insonation location was centered azimuthally with the passive cavitation array. The upstream location was azimuthally located approximately halfway between the center and upstream edge of the passive cavitation array. For all PCIs, a 0.30 MHz band was selected, which corresponded to the −3 dB bandwidth of the fundamental and subharmonic lobes in the power spectrum of the beamformed data at the focus of the Doppler insonation. The PCI in Fig. 3 was formed from the fundamental frequency band (5.85–6.15 MHz). The PCI in Fig. 4 was formed from the inharmonic frequency band (3.85–4.15 MHz). A high acoustic output (MI = 0.80) was used to induce echo-contrast destruction within the tube. The pulse duration was set to 1.33 μs. The cavitation activity mapped to the location of echo-contrast destruction. The flow tube is seen as the bright parallel echoes at depths of 22 and 25 mm. Cavitation activity was also mapped erroneously proximal and distal to the flow tube and constitutes a PCI artifact. This axial artifact has been previously noted.[30] The PCIs were formed using the apodizations A_{Cos} [Eq. (3b)] and A_{NormCos} [Eq. (3d)]. The PCIs created using apodizations A_{Unity} [Eq. (3a)] and A_{Norm} [Eq. (3c)] were very similar to the PCIs created using A_{Cos} and A_{NormCos}, respectively, except that the grating lobes were larger in magnitude for A_{Unity} and A_{Norm}. It should be noted that just six of the sixty-four elements summing constructively yields a −10.3 dB signal, which corresponds to red in the PCIs. Constructive summation on 32 of the 64 elements yields a −3 dB signal, which corresponds to yellow in the PCIs.

Table I reports the −3 dB azimuthal and axial beam widths for the fundamental (5.85–6.15 MHz), subharmonic (2.85–3.15 MHz), and inharmonic (3.85–4.15 MHz) frequency bands using Eq. (2). This is reported for A_{Cos} and A_{NormCos}. The beam widths for A_{Unity} and A_{Norm} differed from A_{Cos} and A_{NormCos}, respectively, by less than 0.1 mm azimuthally and 0.3 mm axially. For the frequency summation that was performed to compute A_{Norm} and A_{NormCos}, all frequencies were used regardless of whether the PCI was formed for the fundamental, subharmonic, or inharmonic acoustic emissions. This was done because the signal in the subharmonic and inharmonic bands of $S_n(\omega)$ was the same magnitude as the system noise floor. The PCIs were formed from acoustic emissions with the pulse Doppler sample volume aligned to the flow tube at the upstream edge of the passive cavitation array, the center of the passive cavitation array, or the downstream edge of the passive cavitation

TABLE I. The –3 dB axial and azimuthal beam widths for the apodizations A_{Cos} and $A_{NormCos}$. Results are shown for beamforming the fundamental (Fund), subharmonic (SH), and inharmonic (IH) frequency bands at three different azimuth cavitation locations.

		Center			Upstream			Downstream		
		Fund	SH	IH	Fund	SH	IH	Fund	SH	IH
Azimuth (mm)	A_{Cos}	0.53	0.61	0.46	0.69	0.61	0.53	0.61	0.69	0.53
	$A_{NormCos}$	0.31	0.53	0.38	0.61	0.69	0.53	0.46	0.69	0.53
Axial (mm)	A_{Cos}	9.16	6.28	5.23	11.52	3.66	3.14	10.99	4.71	3.93
	$A_{NormCos}$	6.02	5.50	4.45	8.38	3.14	2.09	7.59	3.66	2.88

array. Using $A_{NormCos}$ decreased the beam widths relative to A_{Cos} for all cases except the upstream, subharmonic PCI. Despite an improvement in the −3 dB beam widths, $A_{NormCos}$ resulted in a broader distribution of artifact below approximately −6 dB in magnitude, as can be seen in Figs. 3 and 4. Therefore, subsequent results will be reported using A_{Cos}.

Figure 5(A) shows the power spectra at the location of maximum energy in the PCI for pulse Doppler insonation MIs of 0.1, 0.4, and 0.8. These MIs corresponded to insonations with neither stable nor inertial cavitation (no signal above the system noise floor in the subharmonic or inharmonic bands), with predominantly stable cavitation but very minimal inertial cavitation (signal in the subharmonic band approximately 10 dB above the system noise floor but not for the inharmonic band), and with significant stable and inertial cavitation (signal in both the subharmonic and inharmonic bands well above the system noise floor), respectively. Figures 5(B) and 5(C) are PCIs formed from the same data set obtained with an insonation MI of 0.1 but over the subharmonic and inharmonic bands, respectively. Figures 5(D) and 5(E) and Figs. 5(F) and 5(G) are likewise formed but with MIs of 0.4 and 0.8, respectively. All figures were normalized by the data set obtained using an MI of 0.8. Figure 5, demonstrates the ability to independently form PCIs for different types of cavitation activity from the same frames of data.

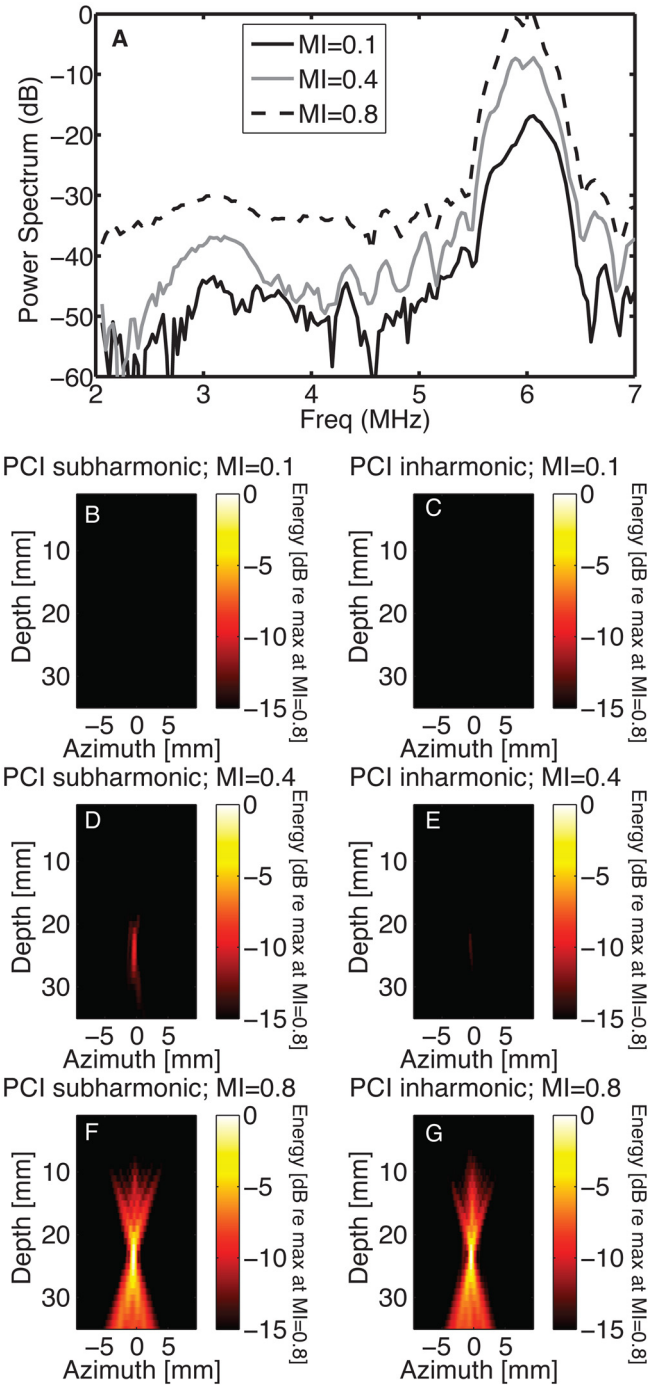

FIG. 5. (Color online) ELIP were insonified with a pulse duration of 1.33 μs for MIs of 0.1, 0.4, and 0.8. Power spectra at the location of the pixel with the maximum amplitude in the PCI (A). PCIs were formed for each MI from the subharmonic band [(B), (D), (F), respectively] and inharmonic band [(C), (E), (G), respectively]. Each image was normalized by the maximum energy in the PCI formed from data obtained while insonifying with an MI of 0.8.

B. Experiment: Pulse duration and envelope

Figures 6 and 7 show PCI data obtained using different sample volume settings, in other words pulse durations, when insonifying filtered, deionized, and degassed water in the flow phantom. The PCI data was formed by summing over the −3 dB bandwidth of the 6 MHz fundamental. The tube was the primary scatterer, which provides a stationary scatting source for all data acquisitions. Figure 6 shows PCIs for insonations of 0.33 μs (Gaussian-windowed) and 8.33 μs (rectangularly windowed). Figure 7 plots the azimuth and range profiles of the PCIs for all available sample volume settings and shows a constant image resolution with changing pulse duration and envelopes. Figures 6 and 7 correspond to scatter off the tube walls since filtered, degassed, and deionized water does not effectively scatter ultrasound. The relatively poor axial resolution prevents the imaging algorithm from resolving the walls separately. Figure 7(A) also plots the Doppler pulse insonation beam pattern in the azimuth direction at the depth of the tube. The insonation beam pattern was measured with a needle hydrophone in a free field. A good correspondence is observed between this measurement and the line profiles formed from the passive imaging algorithm. This provides further confirmation of the spatial accuracy of the passive imaging algorithm. It also demonstrates an alternative method of obtaining beam profile data for calibration purposes.

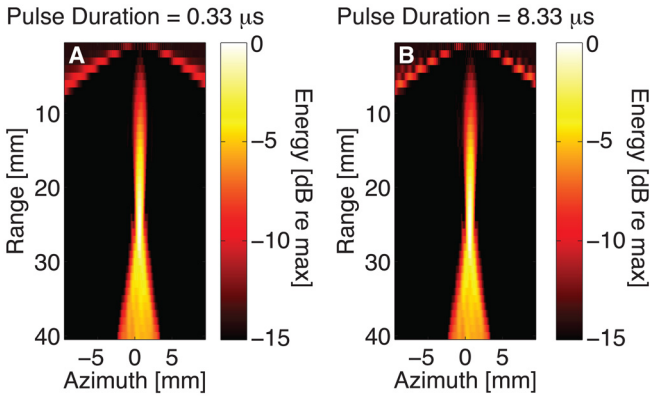

FIG. 6. (Color online) Passive cavitation images from spectral Doppler ultrasound scattered off a flow tube with degassed water at an MI of 0.3. The insonation ultrasound was (A) a 0.33 μs Gaussian-windowed pulse and (B) a 8.33 μs rectangularly windowed pulse. Note that each image was formed from the fundamental band (5.85–6.15 MHz) and normalized to its own maximum and plotted on a dB scale.

Figure 8(A) is an example of a single frame of received radio-frequency data. Figures 8(B), 8(C), and 8(D) are the same data but beamformed to the location of maximum energy in the PCI (azimuth −0.5 mm; range 22 mm), proximal and on-axis with the location of maximum energy in the PCI (azimuth −0.5 mm; range 10 mm), and proximal and off-axis with the location of maximum energy in the PCI (azimuth −4 mm; range 15 mm), respectively.

C. Simulation: Pulse duration and envelope

The experimental results indicated that passive imaging does not depend strongly on insonation pulse duration or envelope. However, it was not possible to look at these two parameters independently with the experimental setup. Therefore investigating them independently was done with

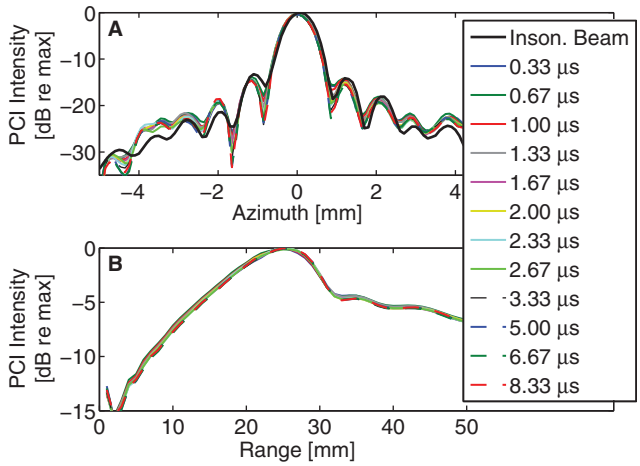

FIG. 7. (Color online) Comparison of line profiles for PCIs with different pulse durations (azimuth and range) and the Doppler insonation beam pattern as measured by a hydrophone (azimuth only). The (A) azimuth and (B) range passive image line profiles are from a depth of 24 mm and azimuthal position of 0 mm, respectively for degassed water in the tube. The insonation duration change is shown in the legend. The pulse envelope was a Gaussian-window for durations of 3.33 μs and less and a rectangular-window for longer durations. The MI was 0.3. The line profiles were formed from the fundamental band (5.85–6.15 MHz).

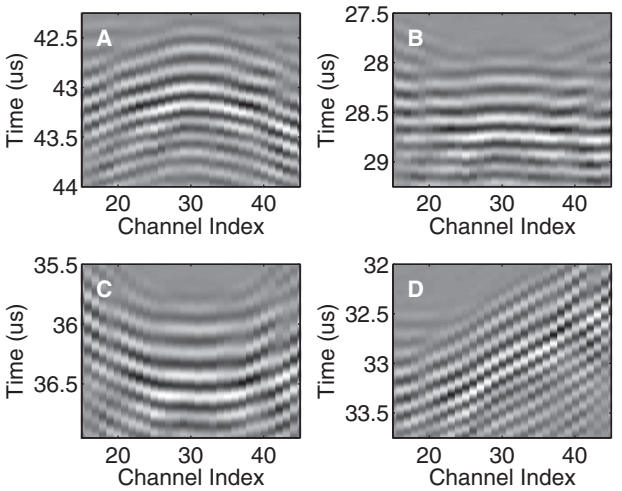

FIG. 8. (A) Sample frame of received experimental radio-frequency data for ELIP insonified at an MI of 0.6 and pulse duration of 0.5 μs. (B) Data beamformed to the location with the maximum energy in the PCI (azimuth of −0.5 mm; depth of 22 mm). (C) Data beamformed for a pixel at a depth of 10 mm but on the axis of cavitation activity. (D) Data beamformed to a location away from the maximum energy in the PCI (azimuth of −3 mm; depth of 15 mm).

simulations. The simulations were performed at 6 MHz, for comparison to the experimental results. Simulations were carried out for 18 different pulse durations ranging from 0.33 μs (two cycles) to 138 μs (equivalent to CW insonation). Figures 9(A) and 9(B) show two example PCIs using rectangularly windowed sinusoids with a duration of 50 and 828 cycles (8.33 and 138 μs), respectively. The shorter duration is the same as the experimental duration in Fig. 6(B). The longer duration corresponded to a CW insonation. No differences were observed in the PCIs until 30 dB below the peak amplitude of the image. Figure 9(C) is formed from a 6 MHz sinusoid with a Gaussian envelope with an equivalent duration of 8.33 μs. The emission was located at a depth of 24 mm and an azimuthal location of 0 mm. This was approximately the same location as the experimental data, except the experimental data had emissions from the proximal and distal walls of the tube. The bandwidth used to form each image was the −3 dB bandwidth of the respective 6 MHz emission waveform. Each PCI was formed using A_{Cos}.

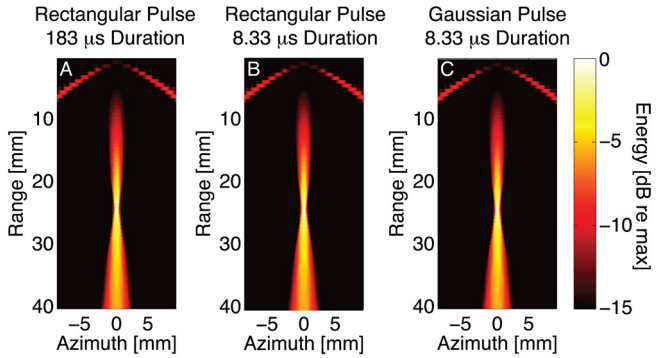

FIG. 9. (Color online) Passive cavitation images formed from the −3 dB frequency band from simulated emissions consisting of a 6 MHz sinusoid windowed with (A) a rectangular window with duration 183 μs, (B) a rectangular window with duration 8.33 μs, and (C) a Gaussian window with an equivalent duration of 8.33 μs.

Differences in the images formed with different pulse envelopes do not appear until 20 dB below the peak. Thus Fig. 9 demonstrates that the PCI point spread function does not substantially change as a function of pulse duration or envelope.

Like the experimental results, the simulated PCI resolution has very little dependence on the emission duration or envelope. Since there is no dependence on pulse duration, one can use a continuous-wave (single-frequency) model to estimate the image resolution as a function of frequency, as would be necessary to estimate the resolution for beamforming the fundamental band, a harmonic band, the subharmonic band, or an inharmonic band. Salgaonkar *et al.*[30] theoretically evaluated passive image resolution in terms of the −6 dB azimuthal point-spread-function width, which was inversely proportional to frequency.

Figure 10 shows that the peak magnitude in the PCI at the source location varies linearly with the energy in the source waveform. This relationship will remain the case for apodizations that only depend on the spatial coordinates, such as A_{Cos}, and broadband, omnidirectional elements in the passive receiving array. This result can be predicted from Eq. (1). At the cavitation source location, the phase-shifts applied in Eq. (1) will adjust $S_n(\omega)$ so that each waveform will sum entirely constructively. As a result, $B(\omega,\vec{x})$ will be a scaled version of the cavitation emission, even if the cavitation emission process is a threshold, nonlinear, or chaotic process. Therefore a linear relationship will exist between the cavitation source energy and the energy in the PCI at the cavitation source. If the transducer elements exhibit significant directivity or frequency sensitivity or a more complex apodization is used, then the linear relationship may break down.

IV. DISCUSSION

Through both experiment and simulation, this study has demonstrated that a passive imaging algorithm can be used to map cavitation activity on an image with resolution that is essentially independent of the duration and envelope of the insonation pulse or cavitation emission. The image amplitude will depend on the duration and envelope. The independence of image resolution can be understood by observing some sample beamformed data. At the source [Fig. 8(B)], the waveforms on each channel are temporally aligned. In comparison, at a location well away from the PCI maximum [Fig. 8(D)], each waveform is shifted in time relative to its neighbor by more than a quarter cycle and less than three-quarters cycle (at which point a grating lobe would begin to appear). As a result there is primarily destructive interference when the waveforms are summed. When beamforming to a location that is proximal or distal to the cavitation emission location [Fig. 8(C)], a subset of channels (channels 25–37) sum constructively, while the remainder do not. Thus elements with a relatively small time-of-flight difference between them for a given pixel location will contribute to the PCI amplitude.

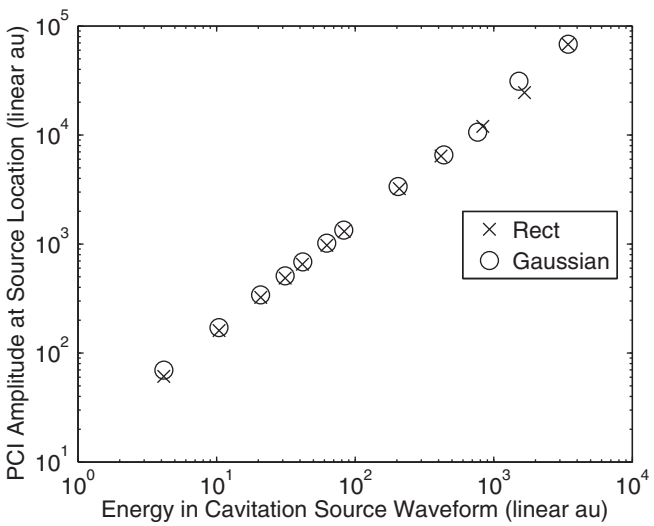

FIG. 10. The magnitude of the simulated PCI image formed from the −3 dB band about 6 MHz at the emission location plotted against the total energy in the cavitation waveform.

Stated another way, coherent interference between delayed and summed waveforms is governed by the wavelength and wavefront curvature, which together determine the frequency-dependent diffraction pattern of the array. The resolution of passive cavitation images thus depends primarily on the center frequency and the array aperture. When the emission duration is decreased, passive cavitation images effectively integrate the image energy $I(\omega,\vec{x})$ over a wider band surrounding the center frequency. The image resolution is thus primarily independent of the cavitation emission duration and envelope.

This result implies that when designing a passive cavitation imaging experiment using a relative phase-difference delay algorithm,[30,32,34] the array design should be the primary factor in determining if adequate image resolution will be obtained. When performing simulations on the array design, a continuous-wave, single-frequency model,[30] which is typically more efficient than pulsed-wave models, can be used without substantial loss of information. If multiple types of cavitation are expected, one may consider modeling a single frequency from each frequency band of interest to ensure adequate resolution for all types of cavitation. This is particularly relevant for low-frequency emissions, which will result in a lower resolution.[30] The low-frequency limitation should also be considered when selecting bands for analysis. When possible, beamforming higher harmonics and ultraharmonics will provide improved resolution. Table I appears to contradict this statement because the 6 MHz band PCI resolutions are larger than the 3 MHz subharmonic band and 4 MHz inharmonic band PCI resolutions. The reason for this is that the reported beam widths are a convolution of the imaging algorithm point spread function and the spatial distribution of the emission sources (i.e., cavitating microbubbles). Because stable and inertial cavitation are threshold phenomena, their spatial distribution is likely smaller than the spatial distribution of microbubbles that exhibit scatter of the fundamental frequency, leading to the smaller apparent resolution.

Orientation of the passive array with respect to the insonation beam pattern is also important to consider. This work confirms the low axial resolution, relative to the azimuthal resolution, observed by Gyöngy *et al.*[32] and Salgaonkar *et al.*[30]

Like the work by Salgaonkar *et al.,* our passive array was placed orthogonal to the direction of insonation, which maximized the resolution. This is often a difficult geometry to achieve *in vivo* and a co-axial arrangement, similar to Gyöngy *et al.* will be needed in many cases. Apodization of the radio-frequency data before beamforming using an energy normalization procedure was explored as one means of improving the axial resolution. However, this technique introduced an "X-type" image artifact. The artifact may be acceptable in cases of focused ultrasound insonation, but is likely unacceptable for bulk ultrasound insonations. Therefore, the continued development of algorithms that improve the axial resolution could be of importance in clinical applications.

The passive cavitation imaging of ultrasound contrast agents in a flow phantom, demonstrated here, shows that the utility of passive imaging extends beyond high-intensity focused ultrasound (HIFU) applications, which have been the focus of prior passive cavitation imaging papers.[30–32] Echogenic liposomes were used solely as cavitation nuclei in this work. However, others have demonstrated that ELIP can be used for localized ultrasound-mediated drug release[43] and delivery.[51] Passive cavitation imaging could be used in these contexts to obtain spatially resolved feedback during a treatment. Optimization of ultrasound insonation pulses based on cavitation emissions has been proposed as an important step in achieving desired bioeffects.[10,52] This may be used for both scanned focused insonations or unfocused bulk ultrasound insonations. As described earlier for passive imaging, it is important to remain cognizant of the algorithm's inability to differentiate between different mechanisms that produce the same frequency content, such as harmonics produced from nonlinear propagation or cavitation emissions.

V. CONCLUSIONS

In summary, it has been shown via experiment and simulation that passive images are essentially independent of the source duration and envelope. The passive image point spread function, however, depends on the frequency band of interest and aperture geometry. The passive cavitation data was shown to localize the cavitation in the azimuth and axial directions properly based on the location of maximum cavitation activity in the PCI. The azimuthal resolution was sufficient to differentiate the mainlobe and sidelobes of the insonation beam. The axial resolution was insufficient to resolve tube walls 2.7 mm apart. An alternative apodization technique based on normalization was used to improve the axial resolution; however, it resulted in additional image artifacts. The energy in the passive image scales linearly with the energy in the source.

ACKNOWLEDGMENTS

This work was supported in part by NIH Grants Nos. F32HL104916, R01HL074002, R01HL059586, and R21EB008483.

[1]C. M. H. Newman and T. Bettinger, "Gene therapy progress and prospects: Ultrasound for gene transfer," Gene Ther. **14**, 465–475 (2007).
[2]S. Hernot and A. L. Klibanov, "Microbubbles in ultrasound-triggered drug and gene delivery," Adv. Drug Delivery Rev. **60**, 1153–1166 (2008).
[3]Y. Zhou, J. Cui, and C. X. Deng, "Dynamics of sonoporation correlated with acoustic cavitation activities," Biophys. J. **94**, L51–L53 (2008).
[4]J. Wu and W. L. Nyborg, "Ultrasound, cavitation bubbles and their interaction with cells," Adv. Drug Delivery Rev. **60**, 1103–1116 (2008).
[5]T. J. Evjen, E. A. Nilssen, R. A. Fowler, S. Røgnavaldsson, M. Brandl, and S. L. Fossheim, "Lipid membrane composition influences drug release from dioleoylphosphatidylethanolamine-based liposomes on exposure to ultrasound," Int. J. Pharm. **406**, 114–116 (2011).
[6]E. C. Everbach and C. W. Francis, "Cavitational mechanisms in ultrasound-accelerated thrombolysis at 1 MHz," Ultrasound Med. Biol. **26**, 1153–1160 (2000).
[7]A. F. Prokop, A. Soltani, and R. A. Roy, "Cavitational mechanisms in ultrasound-accelerated fibrinolysis," Ultrasound Med. Biol. **33**, 924–933 (2007).
[8]S. Datta, C.-C. Coussios, A. Y. Ammi, T. D. Mast, G. M. de Courten-Myers, and C. K. Holland, "Ultrasound-enhanced thombolysis using Definity as a cavitation nucleation agent," Ultrasound Med. Biol. **34**, 1421–1433 (2008).
[9]A. D. Maxwell, C. A. Cain, A. P. Duryea, L. Yuan, H. S. Gurm, and Z. Xu, "Noninvasive thrombolysis using pulsed ultrasound cavitation therapy – histotripsy," Ultrasound Med. Biol. **35**, 1982–1994 (2009).
[10]K. E. Hitchcock, N. M. Ivancevich, K. J. Haworth, D. N. C. Stamper, D. C. Vela, J. T. Sutton, G. J. Pyne-Geithman, and C. K. Holland, "Ultrasound-enhanced rt-PA thrombolysis in an ex vivo porcine carotid artery model," Ultrasound Med. Biol. **37**, 1240–1251 (2011).
[11]H. Tang, C. Chun, J. Wang, D. Blankschtein, and R. Langer, "An investigation of the role of cavitation in low-frequency ultrasound-mediated transdermal drug transport," Pharma. Res. **19**, 1160–1169 (2002).
[12]A. Tezel, A. Sens, and S. Mitragotri, "Investigations of the role of cavitation in low-frequency sonophoresis using acoustic spectroscopy," J. Pharma. Sci. **91**, 444–453 (2002).
[13]A. Tezel and S. Mitragotri, "Interactions of intertial cavitation bubbles with stratum corneum lipid bilayers during low-frequency sonophoresis," Biophys. J. **85**, 3502–3512 (2003).
[14]S. L. Poliachik, W. L. Chandler, R. J. Ollos, M. R. Bailey, and L. A. Crum, "The relation between cavitation and platelet aggregation during exposure to high-intensity focused ultrasound," Ultrasound Med. Biol. **30**, 261–269 (2004).
[15]G. R. ter Haar and C.-C. Coussios, "High intensity focused ultrasound: Physical principles and devices," Int. J. Hyperthermia **23**, 89–104 (2007).
[16]S. D. Nandlall, E. Jackson, and C.-C. Coussios, "Real-time passive acoustic monitoring of HIFU-induced tissue damage," Ultrasound Med. Biol. **37**, 922–934 (2011).
[17]"ANSI technical report: Bubble detection and cavitation monitoring," Technical Report ANSI S1.24 TR-2002, American National Standards Institute Inc., 2007.
[18]A. A. Atchley, L. A. Frizzell, R. E. Apfel, C. K. Holland, S. I. Madanshetty, and R. A. Roy, "Thresholds for cavitation produced in water by pulsed ultrasound," Ultrasonics **26**, 280–285 (1988).
[19]R. A. Roy, S. I. Madanshett, and R. E. Apfel, "An acoustic backscattering technique for the detection of transient cavitation produced by microsecond pulses of ultrasound," J. Acoust. Soc. Am. **87**, 2451–2458 (1990).
[20]M. F. M. Osborne and F. H. Holland, "The acoustical concomitants of cavitation and boiling, produced by a hot wire," J. Acoust. Soc. Am. **19**, 13–29 (1947).
[21]J. McLaughlan, I. Rivens, T. Leighton, and G. ter Haar, "A study of bubble activity generated in ex vivo tissue by high intensity focused ultrasound," Ultrasound Med. Biol. **36**, 1327–1344 (2010).
[22]C.-C. Coussios and R. A. Roy, "Applications of acoustics and cavitation to noninvasive therapy and drug delivery," Ann. Rev. Fluid Mech. **40**, 395–420 (2008).
[23]C. H. Farny, R. G. Holt, and R. A. Roy, "Temporal and spatial detection of HIFU-induced inertial and hot-vapor cavitation with a diagnostic ultrasound system," Ultrasound Med. Biol. **35**, 603–615 (2009).
[24]T. G. Leighton, *The Acoustic Bubble* (Academic, San Diego, 1997), p. 414–420.
[25]E. A. Neppiras, "Acoustic cavitation," Phys. Lett. **61**, 159–251 (1980).
[26]S. Datta, C.-C. Coussios, L. E. McAdory, J. Tan, T. Porter, G. de Courten-Myers, and C. K. Holland, "Correlation of cavitation with ultrasound enhancement of thrombolysis," Ultrasound Med. Biol. **32**, 1257–1267 (2006).
[27]C.-C. Coussios, C. H. Farny, G. R. ter Haar, and R. A. Roy, "Role of acoustic cavitation in the delivery and monitoring of cancer treatment by high-intensity focused ultrasound (HIFU)," Int. J. Hyperthermia **23**, 105–120 (2007).

[28]B. A. Rabkin, V. Zderic, and S. Vaezy, "Hyperecho in ultrasound images of HIFU therapy: Involvement of cavitation" Ultrasound Med. Biol. **31**, 947–956 (2005).
[29]T. D. Mast, V. A. Salgaonkar, C. Karunakaran, J. A. Besse, S. Datta, and C. K. Holland, "Acoustic emissions during 3.1 MHz ultrasound bulk ablation in vivo," Ultrasound Med. Biol. **34**, 1434–1448 (2008).
[30]V. A. Salgaonkar, S. Datta, C. K. Holland, and T. D. Mast, "Passive cavitation imaging with ultrasound arrays," J. Acoust. Soc. Am. **126**, 3071–3083 (2009).
[31]M. Gyöngy, M. Arora, J. A. Nobel, and C.-C. Coussios, "Use of passive arrays for characterization and mapping of cavitation activity during HIFU exposure," IEEE Ultrason. Symp., 871–874 (2008).
[32]M. Gyöngy and C.-C. Coussios, "Passive spatial mapping of inertial cavitation during HIFU exposure," IEEE Trans. Biomed. Eng. **57**, 48–56 (2010).
[33]C. R. Jensen, R. W. Ritchie, M. Gyöngy, J. R. T. Collin, T. Leslie, and C.-C. Coussios, "Spatiotemporal monitoring of high-intensity focused ultrasound therapy with passive acoustic mapping," Radiology **262**, 252–261 (2012).
[34]S. J. Norton and I. J. Won, "Time exposure acoustics," IEEE Trans. Geosci. Remote Sens. **38**, 1337–1343 (2000).
[35]M. Gyöngy and C.-C. Coussios, "Passive cavitation mapping for localization and tracking of bubble dynamics," J. Acoust. Soc. Am. **128**, EL175–EL180 (2010).
[36]D. A. King and W. D. O'Brien, "Comparison bewteen maximum radial expansion of ultrasound contrast agents and experimental postexcitation signal results," J. Acoust. Soc. Am. **129**, 114–121 (2011).
[37]S.-L. Huang, A. J. Hamilton, A. Nagaraj, S. D. Tiukinhoy, M. E. Klegerman, D. D. McPherson, and R. C. MacDonald, "Improving ultrasound reflectivity and stability of echogenic liposomal dispersions for use as targeted ultrasound contrast agents," J. Pharma. Sci. **90**, 1917–1926 (2001).
[38]K. D. Buchanan, S. Huang, H. Kim, R. C. MacDonald, and D. D. McPherson, "Echogenic liposome compostions for increased retention of ultrasound reflectivity at physiologic temperature," J. Pharma. Sci. **97**, 2242–2249 (2008).
[39]J. A. Kopechek, K. J. Haworth, J. L. Raymond, T. D. Mast, S. R. Perrin Jr., M. E. Klegerman, S. Huang, T. M. Porter, D. D. McPherson, and C. K. Holland, "Acoustic characterization of echogenic liposomes: Frequency-dependent attenuation and backscatter," J. Acoust. Soc. Am. **130**, 3472–3481 (2011).
[40]S. Paul, D. Russakow, R. Nahire, T. Nandy, A. H. Ambre, K. Katti, S. Mallik, and K. Sarkar, "In vitro measurement of attenuation and nonlinear scattering from echogenic liposomes," Ultrasonics, doi:10.1016/j.ultras.2012.03.007 (2012).
[41]A. Hamilton, S.-L. Huang, D. Warnick, A. Stein, M. Rabbat, T. Madhav, B. Kane, A. Nagaraj, M. Klegerman, R. MacDonald, and D. McPherson, "Left ventricular thrombus enhancement after intravenous injection of echogenic immunoliposomes: Studies in a new experimental model," Circulation **105**, 2772–2778 (2002).
[42]D. A. B. Smith, T. M. Porter, J. Martinez, S. Huang, R. C. MacDonald, D. D. McPherson, and C. K. Holland, "Destruction thresholds of echogenic liposomes with clincal diagnostic ultrasound," Ultrasound Med. Biol. **33**, 797–809 (2007).
[43]D. A. B. Smith, S. S. Vaidya, J. A. Kopechek, S.-L. Huang, M. E. Klegerman, D. D. McPherson, and C. K. Holland, "Ultrasound-triggered release of recombinant tissue-type plasminogen activator from echogenic liposomes," Ultrasound Med. Biol. **36**, 145–157 (2010).
[44]S.-L. Huang and R. C. MacDonald, "Acoustically active liposomes for drug encapsulation and ultrasound-triggered release," Biochim. Biophys. Acta **1665**, 134–141 (2004).
[45]S.-L. Huang, P. H. Kee, H. Kim, M. R. Moody, S. M. Chrzanowski, R. C. MacDonald, and D. D. McPherson, "Nitric oxide-loaded echogenic liposomes for nitric oxide delivery and inhibition of intimal hyperplasia," J. Am. College Cardiol. **54**, 652–659 (2009).
[46]G. J. Shaw, J. M. Meunier, S.-L. Huang, C. J. Lindsell, D. D. McPherson, and C. K. Holland, "Ultrasound-enhanced thrombolysis with tPA-loaded echogenic liposomes," Thombosis Res. **124**, 306–310 (2009).
[47]M. E. Klegerman, M. Wassler, S.-L. Huang, Y. Zou, H. Kim, H. S. Shelat, C. K. Holland, Y.-J. Geng, and D. D. McPherson, "Liposomal modular complexes for simultaneous targeted delivery of bioactive gases and therapeutics," J. Controll. Release **142**, 326–331 (2010).
[48]L. Y. L. Mo, D. Debusschere, W. Bai, D. Napolitano, A. Irish, S. Marschall, G. W. McLaughline, Z. Yang, P. L. Carson, and J. B. Fowlkes, "Compact ultrasound scanner with built-in raw data acquisition capabilities," IEEE Ultrasonics Symp., 2259–2262 (2007).
[49]L. Y. L. Mo, D. Debusschere, G. McLaughlin, D. Napolitano, W. Bai, K. Fowkes, A. Irish, X. Wang, J. B. Fowlkes, and P. L. Carson, "Compact ultrasound scanner with simultaneous parallel channel data acquisition capabilities," IEEE Ultrasonics Symp, **1**, 1342–1345 (2008).
[50]T. D. Mast, "Fresnel approximations for acoustic fields of rectangularly symmetric sources," J. Acoust. Soc. Am. **121**, 3311–3322 (2007).
[51]K. E. Hitchcock, D. N. Caudell, J. T. Sutton, M. E. Klegerman, D. Vela, G. J. Pyne-Geithman, T. Abruzzo, P. E. P. Cry, Y.-J. Geng, D. D. McPherson, and C. K. Holland, "Ultrasound-enhanced delivery of targeted echogenic liposomes in a novel ex vivo mouse aorta model," J. Controll. Release **144**, 288–295 (2010).
[52]D. E. Goertz, C. Wright, and K. Hynynen, "Contrast agent kinetics in the rabbit brain during exposure to therapeutic ultrasound," Ultrasound Med. Biol. **36**, 916–924 (2010).